ADVANCED FUNCTIONAL MATERIALS
www.afm-journal.de

Gas Sensing of NiO-SCCNT Core–Shell Heterostructures: Optimization by Radial Modulation of the Hole-Accumulation Layer

*Muhammad Hamid Raza, Kaveh Movlaee, Salvatore Gianluca Leonardi, Nicolae Barsan, Giovanni Neri, and Nicola Pinna**

Hierarchical core–shell (C–S) heterostructures composed of a NiO shell deposited onto stacked-cup carbon nanotubes (SCCNTs) are synthesized by atomic layer deposition (ALD). A film of NiO particles (0.80–21.8 nm in thickness) is uniformly deposited onto the inner and outer walls of the SCCNTs. The electrical resistance of the samples is found to increase of many orders of magnitude with the increasing of the NiO thickness. The response of NiO–SCCNT sensors toward low concentrations of acetone and ethanol at 200 °C is studied. The sensing mechanism is based on the modulation of the hole-accumulation region in the NiO shell layer upon chemisorption of the reducing gas molecules. The electrical conduction mechanism is further studied by the incorporation of an Al_2O_3 dielectric layer at NiO and SCCNT interfaces. The investigations on NiO–Al_2O_3–SCCNT, Al_2O_3–SCCNT, and NiO–SCCNT coaxial heterostructures reveal that the sensing mechanism is strictly related to the NiO shell layer. The remarkable performance of the NiO–SCCNT sensors toward acetone and ethanol benefits from the conformal coating by ALD, large surface area of the SCCNTs, and the optimized p-NiO shell layer thickness followed by the radial modulation of the space-charge region.

1. Introduction

Semiconducting metal oxide (SMOX) gas sensors have been successfully used for the purpose of environmental monitoring, public security, sensor networks, automotive applications, domestic safety, chemical quality control, and breath analysis. The development of the new sensing strategies for high sensitivity, rapid response, and superior selectivity are among the major scientific ongoing challenges.[1] Among p-type metal oxides, NiO is one of the most frequently used candidates as active sensing material due to its wide bandgap (3.6–4.2 eV, depending upon the method of preparation and crystallinity), significant change in the electrical properties during chemical reactions on its surface, nontoxicity, high catalytic activity, and low cost.[2] However, the low electronic conductivity of NiO limits its broad applications in chemo-resistive gas sensors.[2d,3] Nonetheless, many approaches have been introduced in the last few years to enhance the gas sensing performance of the NiO-based sensors by i) modifying the size and morphology of the sensing layers,[2a,c,4] ii) synthesizing NiO-based nanocomposites (e.g., with SnO_2, PdO, WO_3, and ZnO),[3,5] and iii) doping NiO with, e.g., Au, Fe, Pt, and Zn.[2b,6] However, these composites may suffer from some issues during the sensing measurements, like aggregation and grain growth at high working temperatures, which cause a reduction in their durability and stability of the electrical response (i.e., baseline shift). Moreover, despite of years of work on metal oxide (MOX) gas sensors, they are still facing shortcomings low selectivity and high working temperature.[7] State-of-the-art NiO sensors are still under active development.[2b,4a,8] One of the options to

M. H. Raza, Prof. N. Pinna
Institut für Chemie and IRIS Adlershof
Humboldt-Universität zu Berlin
Brook-Taylor-Str. 2, 12489 Berlin, Germany
E-mail: nicola.pinna@hu-berlin.de

The ORCID identification number(s) for the author(s) of this article can be found under https://doi.org/10.1002/adfm.201906874.

DOI: 10.1002/adfm.201906874

Dr. K. Movlaee
Center of Excellence in Electrochemistry
School of Chemistry
College of Science
University of Tehran
Tehran 14155-6455, Iran

Dr. K. Movlaee, Dr. S. G. Leonardi, Prof. G. Neri
Department of Engineering
University of Messina
C.Da Di Dio, I-98166 Messina, Italy

Dr. N. Barsan
Institute of Physical and Theoretical Chemistry
University of Tübingen
Auf der Morgenstelle 15, 72076 Tübingen, Germany

overcome these problems is to employ heterostructures made of a CNT core and a metal oxide semiconductor shell. Due to the high surface area and a lower charge recombination rate, the 1D nanostructures, such as nanowires, nanobelts, and nanotubes have exhibited enhanced performances in catalysts and gas sensors as compared to other nanosized composites.[9]

Carbon nanotubes (CNTs) are nanomaterials, which possess a large surface area to volume ratio; hence, they provide a direct benefit for gas sensing applications.[10] However, pristine CNTs are not highly active toward gases and display slow responses and high recovery times.[11] These limitations can be appropriately resolved by designing CNTs-MOX heterostructures, which provide the advantages of both classes of materials without the drawbacks. Indeed, the CNTs provide a suitable conductive platform with a large surface area for metal oxides and a low operating temperature for gas sensing measurements,[10,12] while the metal oxide would provide a high response to analytes. In the recent past, many studies reported improved responses of MOX gas sensors by preparing heterostructures between CNTs and n-type metal oxides, such as SnO_2/CNTs,[13] hex-WO_3/MWCNTs,[14] ZnO/MWCNTs,[15] TiO_2/CNTs,[12] and V_2O_4-CNTs.[16] On the other hand, there are very few reports for p-type metal oxides such as NiO/CNTs heterostructures for gas sensing.[11,17] Even though, some reports demonstrated good sensing properties, the homogeneity, conformality and a proper control over the thickness and particle size of the MOX shell layer onto the CNT walls still remains challenging.

In addition to the nature of the sensing material, porosity and morphology, the shell thickness is also one of the most critical parameters for the design of C-S heterostructures. In particular, when the shell layer thickness is close to the Debye length (λ_D), the conduction is significantly influenced by the modulation of the space charge layer near the interface, which, consequently, leads to the enhanced gas sensing performances.[2d,12,18] Unfortunately, there have not been enough reports on the design of heterostructures with optimized shell thicknesses for gas sensing applications. Generally, solution-based methods show a very limited control over the shell thickness, especially when the shell layer is on the order of few nanometers, hence, alternative methods for preparing conformally coated nanostructures with high aspect ratio and a well-adjusted shell film thickness are needed.

Atomic layer deposition (ALD) has proven to be able to conformally coat high aspect ratio nanostructures with well-calibrated thin films.[18c,19] Our group has already reported a series of heterostructures prepared by ALD for a variety of conformal and homogenous coatings of nanostructured substrates for gas sensing applications.[12,13b,16a,c,18c,19e,20] On the other hand, to the best of our knowledge, there is no report, which studies the role of the NiO shell thickness on gas sensing applications, the electrical conduction mechanism involving MOX-CNTs interfaces and tries to build clear structure-property correlations.

Herein, we report the synthesis of NiO-SCCNTs hierarchical cores–shell (C-S) nanostructures with variable thicknesses of the p-type NiO shell layer by ALD. We dedicated a considerable effort to control the size of the NiO shell layer onto the SCCNT substrate in order to modulate the hole accumulation layer and investigate the effect of this modulation on the gas sensing properties of these nanostructures. Further, a dielectric film of Al_2O_3 was incorporated between the NiO film and the SCCNT substrate to synthesize NiO-Al_2O_3-SCCNTs heterostructures and the electrical conduction mechanism across the NiO and SCCNT interfaces was studied.

2. Experimental Section

Chemicals and Reagents: Stacked-cup carbon nanotubes, SCCNTs (pyrograf III, PR24-PS), were purchased from Applied Science, Inc., nitric acid (67%) was purchased from VWR chemicals. Bis(cyclopentadienyl)nickel (Nickelocene, $Ni(Cp)_2$) was purchased from ABCR GmbH with a purity of 99.99%. Ozone was used as produced by using pure oxygen at a pressure of 1 bar in a BMT803N ozone delivery system. Trimethylaluminum ($(CH_3)_3Al$, TMA, 98%) was purchased from STREM chemicals. Argon was purchased by Air Liquide, 99.99% purity. Other gases, i.e., acetone, ethanol, H_2, NH_3, NO_2, CO_2, CO, and methane were coming from certified bottles purchased from SOL company (www.solgroup.com). All other chemicals and reagents were of analytical grades and used without further purification unless otherwise stated.

Fabrication and Characterization of NiO-SCCNTs and NiO-Al_2O_3-SCCNTs Heterostructures: The comprehensive of the experimental procedure can be found in an earlier report elsewhere.[21] Briefly, stacked-cup carbon nanotubes were treated with nitric acid (HNO_3, 67%) at 105 °C under reflux for 6 h. The mixture was repeatedly washed and filtered with distilled water until the pH = 7. The oxidized SCCNTs were collected and dried in oven at 80 °C for 12 h. Oxidized SCCNTs were coated with NiO by ALD using a hot-wall GEMSTAR-6 Benchtop ALD system (ARRADIANCE, Inc.). The ALD system was evacuated and the temperature was stabilized before starting the deposition. The baseline pressure was maintained at 2.5×10^{-1} torr with a 10 sccm of argon flow. Bis(cyclopentadienyl)nickel ($Ni(Cp)_2$) and ozone (O_3) were introduced in a sequential manner as metal precursor and oxygen source, respectively, while argon was used as carrier and purging gas. The temperature of the $Ni(Cp)_2$ container and the reaction chamber was maintained at 90 and 200 °C, respectively. The pulsing and exposure time for $Ni(Cp)_2$ and ozone was adjusted to 2 s/30 s and 0.5 s/20 s, respectively. Various thicknesses of NiO were deposited by varying the number of ALD cycles (25–700), schematics **Figure 1**a, and the samples were named as *X*NiO-SCCNTs, where *X* stands for the number of NiO ALD cycles (25–700).

Al_2O_3 interfacial layer was deposited using the same ALD setup at the same temperatures as for the NiO deposition (i.e., 200 °C). TMA and Millipore water (H_2O) were used as metal precursor and oxygen source, respectively. Both the precursors were kept at room temperature. Typically one ALD cycle was adjusted as 100 ms pulse, 20 s exposure, and 30 s Ar purging times, alternatively for both the precursors. Various thicknesses of Al_2O_3 were deposited by varying the number of ALD cycles (4–100) and the samples were named as *Y*Al_2O_3-SCCNTs, where *Y* stands for the number of Al_2O_3 ALD cycles. The NiO-SCCNT samples with Al_2O_3 interfacial layers were named as *X*NiO-*Y*Al_2O_3-SCCNTs, where *X* and *Y* represent

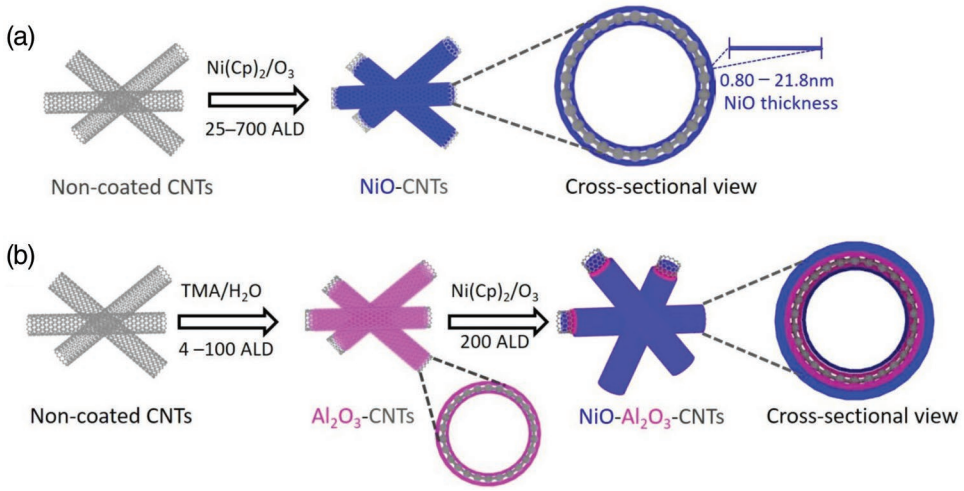

Figure 1. Schematic view of the synthesis process for a) *X*NiO-SCCNTs and b) YAl$_2$O$_3$/SCCNTs and *X*NiO/YAl$_2$O$_3$/SCCNTs heterostructures by ALD.

the number of NiO and Al_2O_3 ALD cycles, respectively (schematics, Figure 1b).

The thickness of the NiO and Al_2O_3 deposited layers was measured on silicon wafers (SSP, Siegert wafer B014002) using SENpro spectroscopic ellipsometer from Sentech. The data were collected at an incident angle of 70° with a wavelength range from 370–1000 nm and fitted to the model using the SpectraRay 4 software. For the characterization of the NiO-SCCNTs and *X*NiO-YAl$_2$O$_3$-SCCNT samples, transmission electron microscopy (TEM), and selected area electron diffraction (SAED) were carried out on a Philips CM 200 TEM equipped with a LaB_6 filament at an acceleration voltage of 200 kV. High-resolution transmission electron microscopy (HRTEM), high-angle annular dark-field scanning transmission electron microscopy (HAADF-STEM), and energy dispersive X-ray analysis (EDX) elemental mapping were performed by an FEI Talos F200S scanning/transmission electron microscope (S/TEM), operated at 200 kV. X-ray photoelectron spectroscopy (XPS) was performed in an ultrahigh vacuum chamber (base pressure 5×10^{-10} mbar) using a JPS-9030 photoelectron spectrometer hemispherical energy analyzer and a nonmonochromatic Al $K\alpha$ ($h\nu$ = 1486.6 eV) X-ray source. The energy resolution was 0.9 eV as determined from the full-width half-maximum of the Ag $3d_{5/2}$ measured on a polycrystalline silver substrate. Powder X-ray diffraction (p-XRD) patterns were obtained on a STOE Stadi MP diffractometer with Mo $K_{\alpha 1}$ radiation source (λ = 0.7093 Å) operating at 40 KV.

Gas Sensing Tests: Sensors were fabricated by depositing a film of the water dispersed *X*NiO-SCCNT samples onto the platinum interdigited area of alumina substrates (6×3 mm^2) containing a Pt heater located on the backside. After that, sensors were introduced in a stainless-steel chamber for the sensing measurements. The experimental bench for the electrical characterization of the sensors allows to carry out measurements in a controlled atmosphere. Gases coming from certified bottles were diluted in air at a given concentration by mass flow controllers. All the measurements were carried out at 200 °C, under a dry air total stream of 100 sccm. A multimeter data acquisition unit Agilent 34970A was used for this purpose, while a dual-channel power supplier instrument Agilent E3632A was employed to bias the built-in heater of the sensor to perform measurements at super-ambient temperature. The sensor response (S) is defined as $S = R_g / R_a$, where R_g and R_a are the electrical resistance values of the sensor in the presence and absence of target gases, respectively. Detail of the sensor fabrication and measurements can be found in earlier reports.[22]

3. Results and Discussion

3.1. Morphological and Microstuctural Characterization of NiO-SCCNT Heterostructures

The relative thickness of the NiO ALD film on Si-wafers was initially measured by ellipsometry. Well-cleaned Si-wafers were coated in the ALD chamber at the same time as the SCCNTs. Ellipsometry data confirmed the successful execution of the ALD process, by comparing the thickness of the coated silicon wafer to the noncoated wafer. The fits of the data in Figure S1 (Supporting Information) show that the curves move systematically to a comparatively lower delta value with the increasing of the number of ALD cycles. The growth per cycle (GPC) was consistently determined in terms of thickness of the NiO deposited layer versus the number of ALD cycles on Si/SiO_2 wafers. The growth is highly linear (R^2 = 0.996) with a GPC of 0.37 Å as estimated from the slope of the linear fit (Figure S1, Supporting Information).

The structure and morphology of the NiO-SCCNT samples were thoroughly analyzed by TEM. Figure S2a–d (Supporting Information) shows overview TEM images of some noncoated SCCNTs and NiO coated SCCNTs. **Figure 2** shows HRTEM images for the samples coated by 100, 200, 400, and 700 NiO ALD cycles. Some additional HRTEM images to differentiate between the thickness of the NiO shell layer for the SCCNT samples coated with 25, 50, 100, 200, 400, and 700 NiO ALD cycles can also be found in our recent report.[21] It can be seen that the SCCNTs are equally and conformally coated from

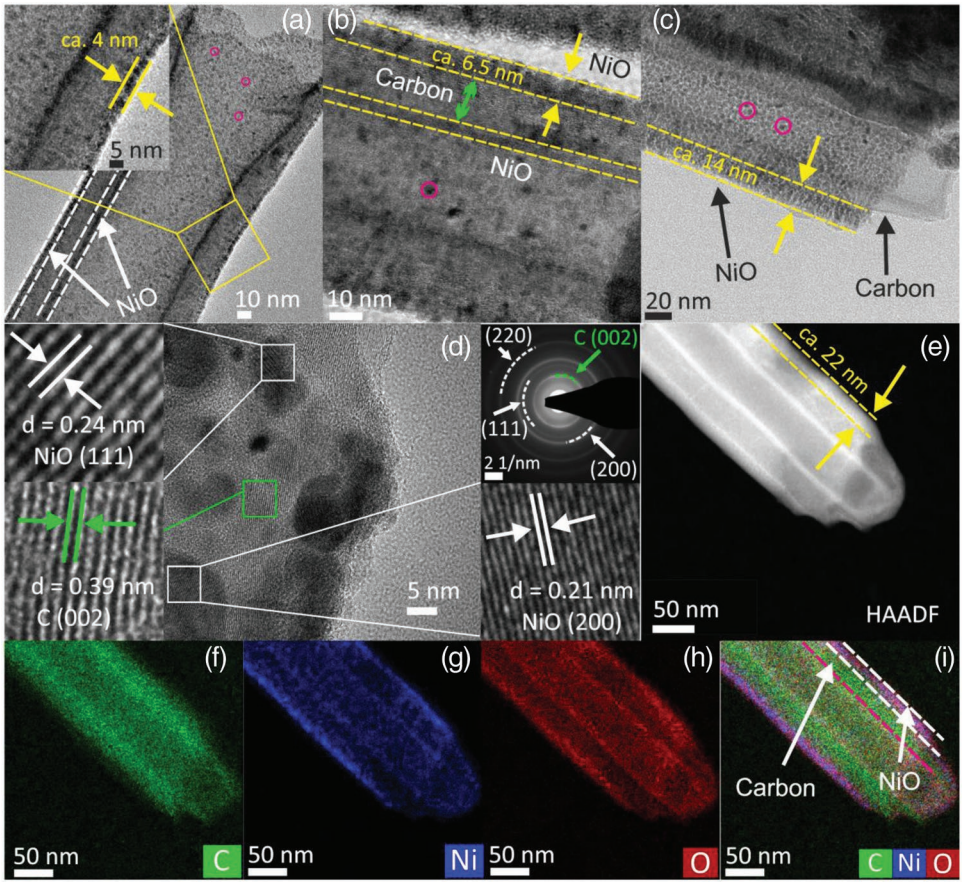

Figure 2. High-resolution transmission electron microscopy (HRTEM) images of a) 100NiO-SCCNTs, b) 200NiO-SCCNTs, c) 400NiO-SCCNTs, d) magnified HRTEM image of the 200NiO-SCCNTs sample, e) HAADF-STEM images of 700NiO-SCCNTs, and f–i) the corresponding EDX elemental mappings for carbon, nickel, oxygen, and all combined, respectively. The thickness marked is calculated using the DigitalMicrograph software.

the inner and the outer surfaces with NiO nanoparticles. It is observed that small NiO nanoparticles were deposited after 25 ALD cycles with a steady growth to a compact and dense NiO film with increasing the number of ALD cycles. The thickness of the NiO coating increases with the number of ALD cycles (Figure 2a–c,e and Figure S2f–I, Supporting Information). The GPC determined from the thickness of the NiO films grown on the SCCNTs for various number of ALD cycles is almost constant. The linear fitting (R^2 = 0.993) of the NiO thickness versus the number of ALD cycles passes by the origin with a slope of 0.32 Å cycles^{-1} corresponding to a GPC of 0.32 Å cycles^{-1}, as also reported recently by us.[21] The average thickness calculated for the NiO-SCCNT samples from TEM images are similar to the values calculated from ellipsometry data (**Table 1** and Figure S1, Supporting Information). This further proves the ALD character and the self-terminating behavior of the process under the applied conditions, indicating that the thickness of the NiO shell layer can be tailored by controlling the number of ALD cycles. Further, HRTEM, HAADF-STEM, bright-field (BF), and EDX mappings images are shown in Figure 2. The lattice spacing of 0.21 and 0.24 nm in magnified HRTEM can be assign to the interplanar distance of the (111) and (200) lattice planes for the NiO, whereas the spacing of 0.39 nm can be assigned to the (002) plane of hexagonal graphitic carbon, respectively. The concentric rings in the SAED obtained for 200NiO-SCCNTs confirm the polycrystalline characteristic of the NiO coating (inset of Figure 2d). The main Debye-Scherrer rings correspond to the (200), (111), and (220) planes of the rock salt structure of NiO (ICDD 08-089-7130) and to the (002) plane for graphitized carbon (ICDD 01-075-1621). It can be seen in the HAADF-STEM and in the corresponding elemental mappings images that NiO is homogenously distributed throughout the inner and outer walls of the SCCNT forming a smooth and conformal layer (Figure 2e–i).

The structure and phase composition of the sample were studied by X-ray diffraction (XRD). Figure S3 (Supporting Information) shows the XRD patterns for the pristine SCCNTs, 200NiO-SCCNTs, $4Al_2O_3$-SCCNTs, $100Al_2O_3$-SCCNTs, and 200NiO-$4Al_2O_3$-SCCNTs heterostructures. The SCCNTs (black) sample shows reflections at 11.9° and 20.02° (2θ), which can be attributed to the (002) and (101) planes of graphitic carbon, respectively (ICDD 01-075-1621 (Carbon)). It can be seen that all the NiO containing samples (i.e., NiO/Al_2O_3/SCCNTs and Al_2O_3/SCCNTs) show the distinct diffraction signals located at 16.8°, 19.5°, and 27.7°, corresponding to the (111), (200), and (220) reflections of the face-centered cubic, rock-salt (NaCl-type), NiO structure, respectively (space group: $Fm\bar{3}m$ (225), ICDD 08-089-7130). In addition, all the NiO and Al_2O_3 coated

Table 1. Summary of the ALD deposited NiO shell layer thickness and growth per cycles (GPC) as calculated by transmission electron microscopy (TEM) on SCCNTs and ellipsometery on silicon wafers.

Number of ALD cycles	Transmission electron microscopy (TEM)			Ellipsometry		
	Thickness [nm]	GPC [Å per cycle]	Slope of the linear fit (GPC)	Thickness [nm]	GPC [Å per cycle]	Slope of the linear fit (GPC)
25	0.8	0.32	0.32 Å per cycle	0.74	0.29	0.37 Å per cycle
50	1.7	0.34		1.89	0.37	
100	4.0	0.4		3.42	0.34	
200	6.5	0.32		7.08	0.35	
400	14.0	0.35		16.04	0.4	
700	21.8	0.31		24.43	0.34	

samples show the characteristic graphitic carbon signal (002) at 11.9°, marked with asterisk. It can be seen that both, NiO/Al_2O_3/SCCNTs and Al_2O_3/SCCNTs, did not show any reflection that can be assigned to the Al_2O_3 showing the amorphous nature of the ALD deposited Al_2O_3 film. Moreover, all the NiO-SCCNTs heterostructures with 50, 100, 200, and 400 deposition cycles of NiO show the diffraction peaks corresponding to the reflections of face-centered cubic NiO, but with higher number of ALD cycles the reflection from the SCCNTs becomes less pronounced compared to the reflections originating from NiO, reported in our previous article.[21]

The chemical state of the NiO film deposited on SCCNTs was examined by high-resolution XPS.[5a] **Figure 3**a displays the Ni $2p_{3/2}$ core level spectra for the NiO-SCCNT samples with 100, 200, and 700 ALD cycles. The broad feature centered at 861.2 eV is mainly due to the complex multiplet splitting and to the number of possible final states due to the strong overlap of the Ni and O orbitals. More relevant is the low BE peak centered at 854.1 eV, which can be unambiguously ascribed to Ni^{2+} in the NiO_6 octahedral coordination of the cubic rock-salt NiO structure.[23] The remaining peak at 856.2 eV is known to be a surface component and can be attributed to surface hydroxylated NiO, similarly to Ni^{2+} in $Ni(OH)_2$.

Figure 3b presents the O1*s* edges of NiO deposited onto SCCNTs with 100, 200, and 700 ALD cycles. The lower binding energy peak at 529.5 eV is representative of the lattice oxygen, i.e., O^{2-} in NiO. At high binding energy, the small peak at 533.2 eV corresponds to residual water at the film surface. The peak at 531.5 eV can be indexed to surface hydroxyl groups.[24] In the present study, all deposition were executed in a moisture free highly evacuated chamber using argon as a carrier and purging gas for the precursors, so, the hydroxylated surface should be due to the short exposure in air after deposition. On the other hand, the bulk of the film still remains rock salt NiO (cf. XRD,[21] TEM, and SAED results above) while the surface has been hydroxylated over the top few nanometers.

It can also be further observed for both, Ni 2p and O 1s, regions that the NiO contribution became more prominent

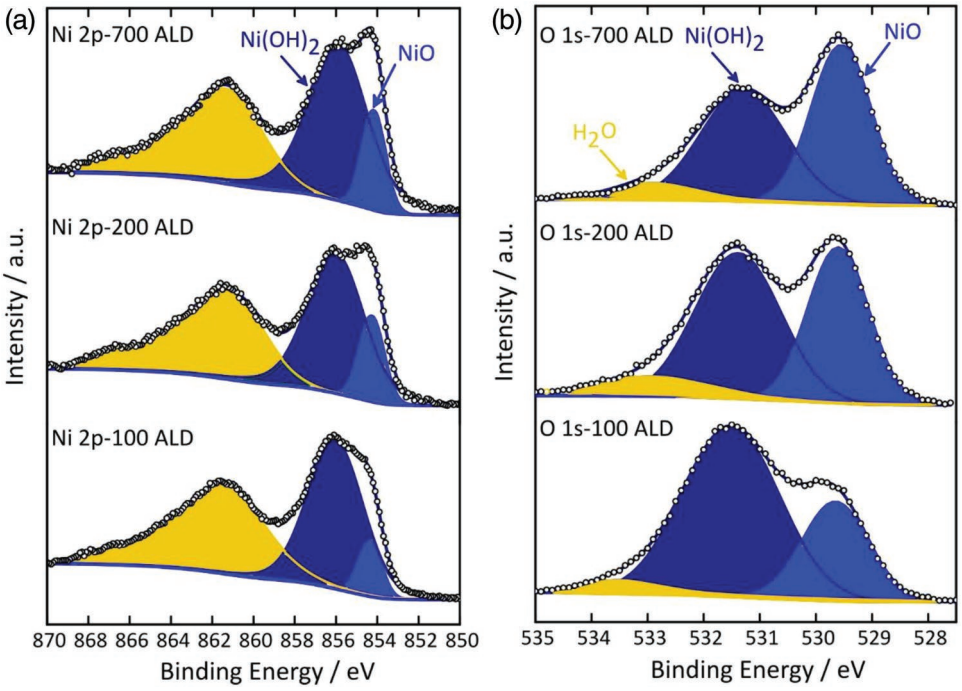

Figure 3. High-resolution XPS spectra of NiO-SCCNT samples with 100, 200, and 700 ALD cycles, a) Ni 2p, and b) O 1s scanned regions.

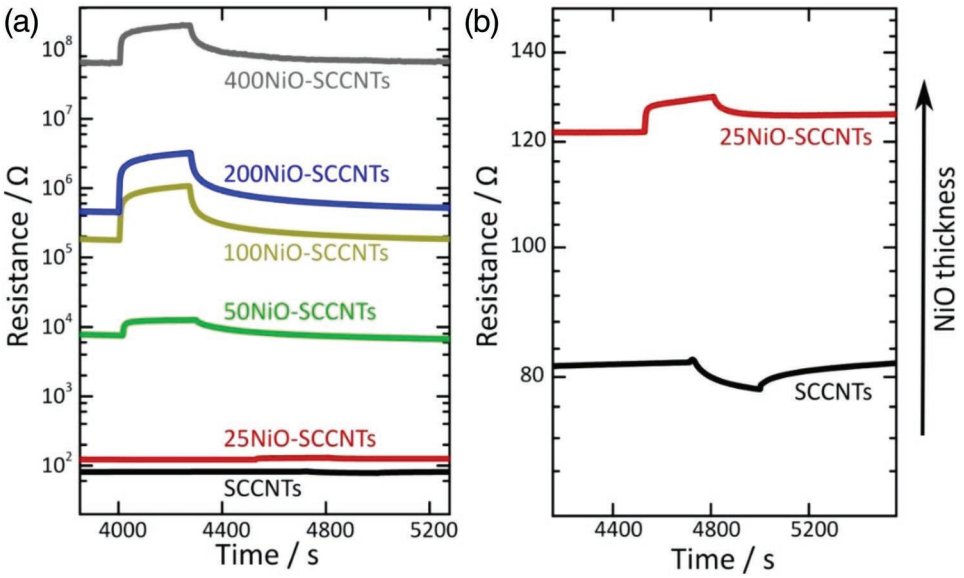

Figure 4. a) Baseline resistance (R_a) variation to a 10 ppm pulse of ethanol of the oxidized SCCNTs and *X*NiO-SCCNTs sensors, b) enlarged view of the SCCNTs (black) and 25NiO-SCCNTs (red) sensors.

with the increasing of the number of ALD cycles. Since the thickness of NiO coating increases with the increasing of the number of ALD cycles, hence the bulk component (NiO) became more prominent than the hydroxylated surface region.

3.2. Electrical Characteristics

Electrical and sensing characteristics of the NiO-SCCNT C-S heterostructures were evaluated with the planar conductometric sensor device, described in our previous reports.[20a] **Figure 4**a,b reports the response to 10 ppm of ethanol in dry air at 200 °C for the oxidized SCCNTs and all the *X*NiO-SCCNT fabricated sensors. First, we can note the strong baseline resistance (R_a) difference among the various sensors. The SCCNT sensor showed a very low value of R_a, i.e., about 82 ohm, which is in accordance to the relatively high conductivity of the carbon nanotubes.[13b] **Figure 5** shows the schematic of the cross-sectional view for the NiO-SCCNTs based device and the expected corresponding electron-flow channel. The baseline resistance (R_a) of *X*NiO-SCCNT sensors increased with the increasing of the NiO thickness, which shows that the resistance of NiO-SCCNT sensors largely depends on the thickness of the NiO shell layer (**Figure 6**a). The 700NiO-SCCNT sensor showed a high resistance value, approximately up-to seven-order of magnitude as compared to the oxidized SCCNTs. Due to the very low resistance of the SCCNTs, it is reasonable to expect that the electrical current will all the time cross the junction between them and the NiO shell; moreover, because the current cannot pass from one NiO-SCCNT element to the other without crossing the NiO layer, it is reasonable to expect that the conduction path can be described by a series arrangement of three resistive elements: the SCCNTs, the junction between them and the NiO shell, and the NiO shell. Hence, the resistance of the *X*NiO-SCCNT sensors is dominated by the resistive shell layer and/or the heterojunction formed between it and the SCCNTs, rather than the semiconducting core substrate; the reason is that these three resistive elements are placed in series and in such an arrangement the large resistances dominate.

Reversible variations in the baseline resistance were observed in the presence of ethanol, indicating that these devices can be used as sensors. Furthermore, the response to target gas appears to be linked to the thickness of the NiO coating. A deeper discussion about this behavior is reported in the next section.

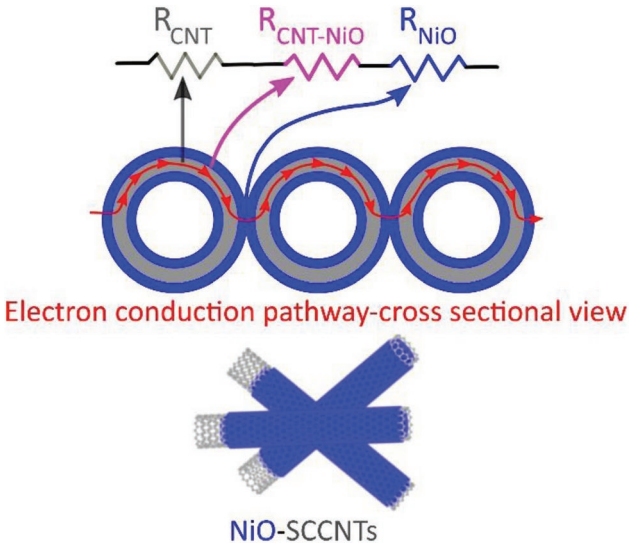

Figure 5. Schematics of the resistive elements in series and the corresponding cross-sectional view of the electron-flow channel into the NiO-SCCNTs nanostructures.

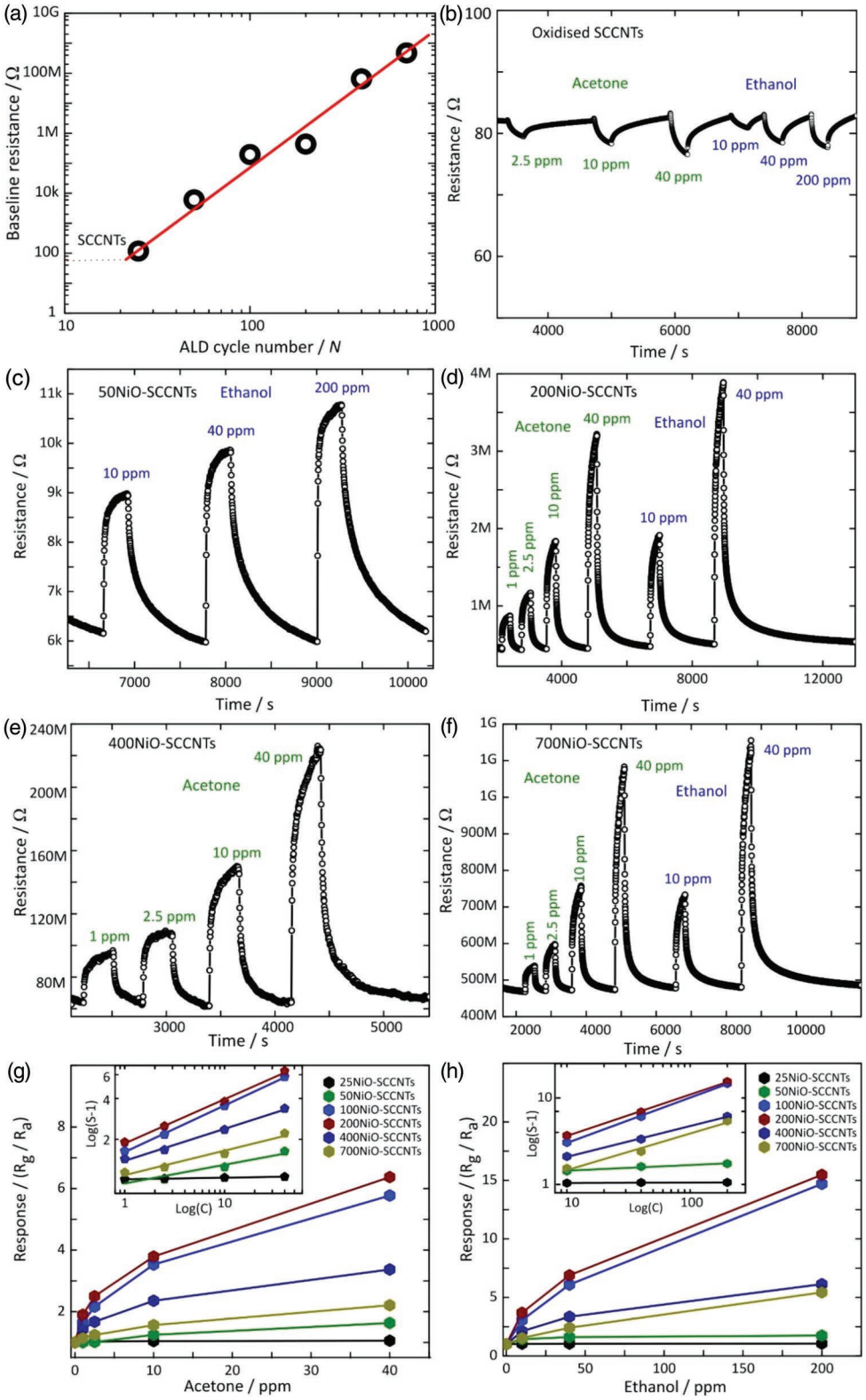

Figure 6. a) The linear plot of the baseline resistance versus the number of ALD cycles (NiO shell thickness) of *X*NiO-SCCNTs and SCCNTs sensors. Dynamic response toward different concentrations of acetone and ethanol at 200 °C by the fabricated sensors with, b) oxidized SCCNTs, c) 50NiO-SCCNTs, d) 200NiO-SCCNTs, e) 400NiO-SCCNTs, and f) 700NiO-SCCNTs. The Response variations of *X*NiO-SCCNTs sensors for different concentrations of target gases, g) acetone and h) ethanol. The insets in (g) and (h) show the linear fit of the logarithmic expression of the *X*NiO-SCCNT sensors response as a function of the target gas concentrations. All the tests were performed at 200 °C.

3.3. Gas Sensing Tests

The gas sensing properties of the SCCNTs and *X*NiO-SCCNTs C-S heterostructures were investigated to evaluate their applicability toward acetone and ethanol gas detection. A temperature of 200 °C was chosen for this study, which is similar to the already optimized and reported temperatures for the NiO and CNTs composites.[11,17] The gas sensing tests were performed for acetone and ethanol with the oxidized SCCNTs and a series of *X*NiO-SCCNT sensors in an especially design sensing chamber and the variations in the resistance (R_g) were registered. Figure 6b–e represents the response of all the sensors to various concentrations of acetone and ethanol at 200 °C. When acetone and ethanol were introduced in the sensing chamber, the resistance of the SCCNTs decreases and shortly reached a minimum resistance value, which indicate an n-type response of the oxidized SCCNTs (Figure 6b). Generally, CNTs are reported as a p-type semiconductor, even though, it has been reported that depending on the procedure of synthesis and pre-treatment as well as the presence of even very small amount of impurity of metal/metal oxide, this semiconducting behavior may change. Especially, the electronic properties of the CNTs are very sensitive to the chemical environment and conditions. It was demonstrated that the electrical resistance and local density of states of the CNTs are influenced by its exposure to a certain environment and these can be tuned reversibly by even small concentrations of adsorbed gases. The electronic properties of the CNTs are not only related to the diameter and chirality, but also depend on the gas history as well.[25] In particular, it has been found that the degree of oxygen exposure is the determining factor as to whether a carbon nanotube functions as an n-type or p-type semiconductor.[25b]

The dynamic response of the *X*NiO-SCCNT sensors toward various concentrations of acetone and ethanol (from 1 ppm to 40 ppm) as target gases is shown in the Figure 6c–f. It can be seen that coating of the NiO shell layer on the SCCNTs (NiO-SCCNTs C-S heterostructures) remarkably modified the semiconducting nature of the SCCNTs. In response to acetone and ethanol, the resistance of the *X*NiO-SCCNT sensors increases and then recover promptly to the baseline value as the gases are removed from the testing chamber. The responses of the NiO-SCCNTs materials show a typical p-type behavior. Because the NiO shell is very compact, the reaction with the gases will take place at its surface. The corresponding changes in the surface charge could determine changes of all resistive elements, namely: NiO shell, heterojunction formed between the shell and the SCCNTs and the resistance of the SCCNTs. As explained above, because these resistive elements are placed in series the ones showing the larger values dominate. The two candidates are the NiO shell and the heterojunctions.

The reasons for the changes of the surface charge are related to the interaction with the gases present in the atmosphere. When a material is exposed to air, the oxygen molecules adsorbed on the NiO surface capture electrons forming negatively charged (O_2^-, O^-, and O^{2-}) surface species. For NiO, which is a p-type material, the resistance at the surface decreases due to the increase of the carrier density (hole-accumulation layer, HAL). On exposure to a reducing gas like acetone and ethanol, the gas molecules react with the adsorbed oxygen (oxidize to, e.g., CO_2 and H_2O) leading to the release of electrons back to the surface. These electrons combine with the holes in the p-type material causing a reduction in the carrier concentration and therefore to an increase in resistance.[26]

The changes in the free charge carrier concentration in the NiO layer could also influence the resistance of the other possible candidate, as a dominant resistive element, namely the heterojunction formed between the shell and the SCCNT. This can happen only in the case in which the influence of the surface reactions extends in the full shell, i.e., shell thickness comparable to the Debye length (λ_D). In the case of larger shell thicknesses one would expect that, besides the lack of influence on the properties of the heterojunction, also the sensor signals would be decreased; the reason is that the shell will present two different regions, the surface accumulation layer, the resistance of which will depend on the ambient atmosphere composition, and the bulk region, the resistance of which won't be changed (cf. Figure 5). Because these two contributions to the NiO shell resistance will be placed in series, a large contribution of the bulk will decrease the overall change of the resistance, which is the sensor signal.

The gas sensing response of the *X*NiO-SCCNT sensors increased with the increasing of the concentration of the target gases (Figure 6g,h). The linear dependence of the gas response (S) to the concentration of the target gases can be represented empirically by $S = a[C]b+1$ or $\log (S - 1) = b\log [c] + \log(a)$.[29] The inset of Figure 6g,h indicates that all the *X*NiO-SCCNT sensors have excellent linearity (determination coefficient, $R^2 > 0.98$) in logarithmic form and these NiO-SCCNTs hierarchical C-S nanostructures can be used as promising sensing materials for acetone and ethanol detection.

The experimental results show that there is a correlation between the NiO shell thickness (i.e., the number of ALD cycles) of the *X*NiO-SCCNTs C-S nanostructures and their gas sensing response. It implies that the sensing property of NiO-SCCNTs nanostructures is intimately linked to the width of the depletion layer. Surprisingly, at a first glance, the response (*S*) initially increased as the NiO thickness increased from 0 to about 5–6.5 nm (200 ALD cycles) and then decreases progressively for the thicker films grown with 400 and 700 ALD cycles (≈14 and 22 nm shell thickness) (**Figure 7**). The high sensing response of the 200NiO-SCCNT sensor is due to the fact that the thickness of the NiO coating is similar to the thickness of the depletion layer, *i.e.*, few times of the Debye length (λ_D).[23c] At this point, the entire film is in the space-charge-region and the charge conduction in the NiO film is dominantly perturbed by the oxygen species and/or acetone/ethanol chemisorbed at the surface.[27,2d] The decrease of the sensor signal when the thickness increases is easy to understand because of the increasing contribution of the bulk region and because the decrease starts around a thickness between 6 and 8 nm corresponding to the similar or few order-of-magnitude of the Debye length. The initial increase is more puzzling because one expects that at thickness below the Debye length the effect of the surface accumulation layer fully dominates. There are three possible reasons:

- There is a pinning of the Fermi level at the interface between the shell and the SCCNT, like in the case of the contact

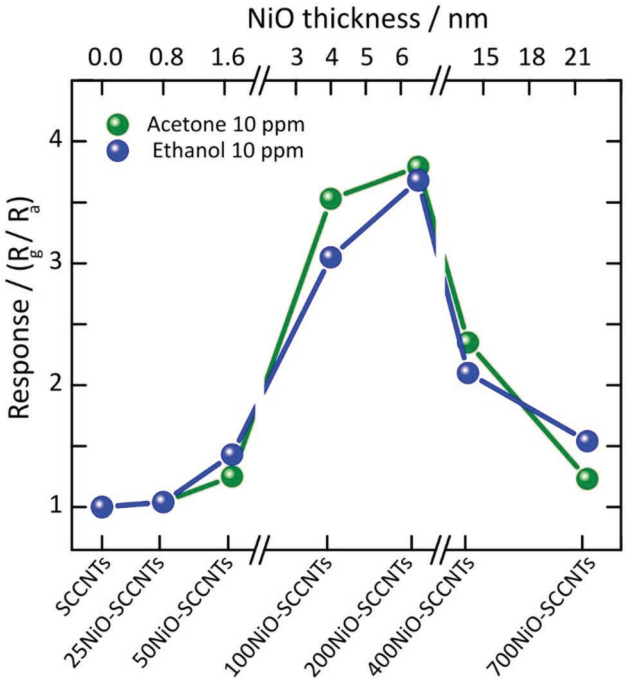

Figure 7. NiO shell layer thickness of *X*NiO-SCCNT sensors as a function of the sensing response toward acetone and ethanol at 200 °C, showing a change in sensing response with varying the NiO shell thickness.

resistance between electrodes and SMOX explained by Barsan et al.[28] This would mean that the resistance of the heterojunction will be determined by the bulk properties of the SCCNT and the NiO, e.g., will not depend on what happens at the surface of the NiO shell. If this contribution is large, it will limit the sensor signal.

- The surface reactivity with oxygen depends on the availability of free charge carriers in the NiO shell. It is possible that at low thicknesses, the low number of charge carriers limits the surface ionosorption of oxygen. Less ionosorbed oxygen will determine less reaction partners for the reducing gases and lower sensor signals.
- A third possibility could be that at very low number of ALD cycles the NiO films is not conformal and therefore some CNTs-CNTs junctions, i.e., not mediated by NiO, could exist. These pinholes can be due to the fact that NiO is deposited as a crystalline nanoparticulate films in contrast to the conformally grown film of amorphous Al_2O_3 even for few ALD cycles (cf. below and **Figure 8**a). Indeed, for a low number of ALD cycles (25–50), only very small NiO particles forming a noncontinuous films are visible in the TEM images (Figure S2f,g, Supporting Information). With the increasing of the numbers of ALD cycles, the particles size increased forming a smooth and conformal polycrystalline layer over the SCCNT substrates (Figure 2a–c and Figure S2g–I, Supporting Information)

The extremely strong dependence of the sensor resistance on the NiO shell thickness, which seems to extrapolate to values very close to the resistance of the SCCNT, suggests that the resistive contribution of the heterojunction is not too high so, most probable the second and the third reasons are operating in this case.

The electrical charge transfer process (transduction function) at the different interfaces across the NiO-SCCNTs heterostructures was further examined by incorporating an Al_2O_3 thin film with various thicknesses (as a *k*-dielectric interfacial layer) between the NiO and the SCCNT substrate. The evaluation of the presence of an insulating layer of Al_2O_3, able to isolate spatially and electrically the NiO sensing layer from the conductive SCCNT substrate, has been carried out by electron microscopy and electrical measurements. The study was performed by developing *X*NiO-*Y*Al_2O_3-SCCNTs heterostructures (cf. schematics in Figure 1b). Different thicknesses of Al_2O_3 were deposited directly onto the pristine SCCNTs, while the thickness of NiO was kept constant as for the best performing sample for sensing, i.e., 6.2 nm (200NiO-SCCNTs, 200 ALD cycles).

Figure S4 (Supporting Information) shows the HAADF-STEM and the corresponding EDX elemental mappings images of the 4Al_2O_3/SCCNTs. It can be seen that Al_2O_3 is homogenously and conformally deposited onto the SCCNTs. Figure 8a,c shows the BF-TEM and HAADF-STEM images for the 4Al_2O_3-SCCNTs and 100Al_2O_3-SCCNTs C-S heterostructures, respectively. NiO is deposited homogenously on the alumina surface with a similar thickness as for the 200NiO-SCCNTs heterostructures (Figure 8b). Figure 8d–f shows HAADF-STEM images for the 200NiO-4Al_2O_3-SCCNTs, 200NiO-19Al_2O_3-SCCNTs, and 200NiO-100Al_2O_3-SCCNTs, respectively. It can be seen that NiO is deposited on all the nanostructures with a similar thickness while varying the thickness of the interfacial alumina layer. The thickness increases of the Al_2O_3 film from 4 to 100 ALD cycles in *X*NiO-*Y*Al_2O_3-SCCNTs heterostructures are nicely demonstrated by the EDX elemental maps (Figure 8g–i). It can also be seen that Al_2O_3 ALD ultimately blocks the inner walls for NiO deposition at 100 ALD cycles (Figure 8f,i). Hence, for the 200NiO-100Al_2O_3-SCCNTs heterostructures, the NiO is present only on the outer walls of the SCCNTs and alumina is deposited homogenously both in the outer and inner walls of the CNTs (Figure 8i).

The effect of the Al_2O_3 film on the electrical characteristics of pristine SCCNTs and as an interfacial layer between the NiO thin film and SCCNTs interfaces was first investigated by measuring the baseline resistance. Baseline resistance of the 100Al_2O_3-SCCNTs and even for the 19Al_2O_3-SCCNT samples was very high, higher than the detection limit of our instrument. This is due to the elevated resistance of the Al_2O_3 layer precluding any further measurements. This also proves that the Al_2O_3 film is conformal. However, the resistance of the heterostructures with 4-ALD cycles of Al_2O_3 was in the measurable range and afterward all the experiments were only performed with the samples with 4 Al_2O_3-ALD cycles. **Figure 9**a shows the resistance variation for the SCCNTs, 200NiO-SCCNT, 4Al_2O_3-SCCNT, and 200NiO-4Al_2O_3-SCCNT samples during heating from room temperature to 200 °C in air. The NiO containing heterostructures show a typical semiconducting behavior. The resistance of the SCCNTs covered with just 4 ALD cycles (4Al_2O_3-SCCNTs) increases of approximately eight orders-of-magnitude as compared to the pristine SCCNTs,

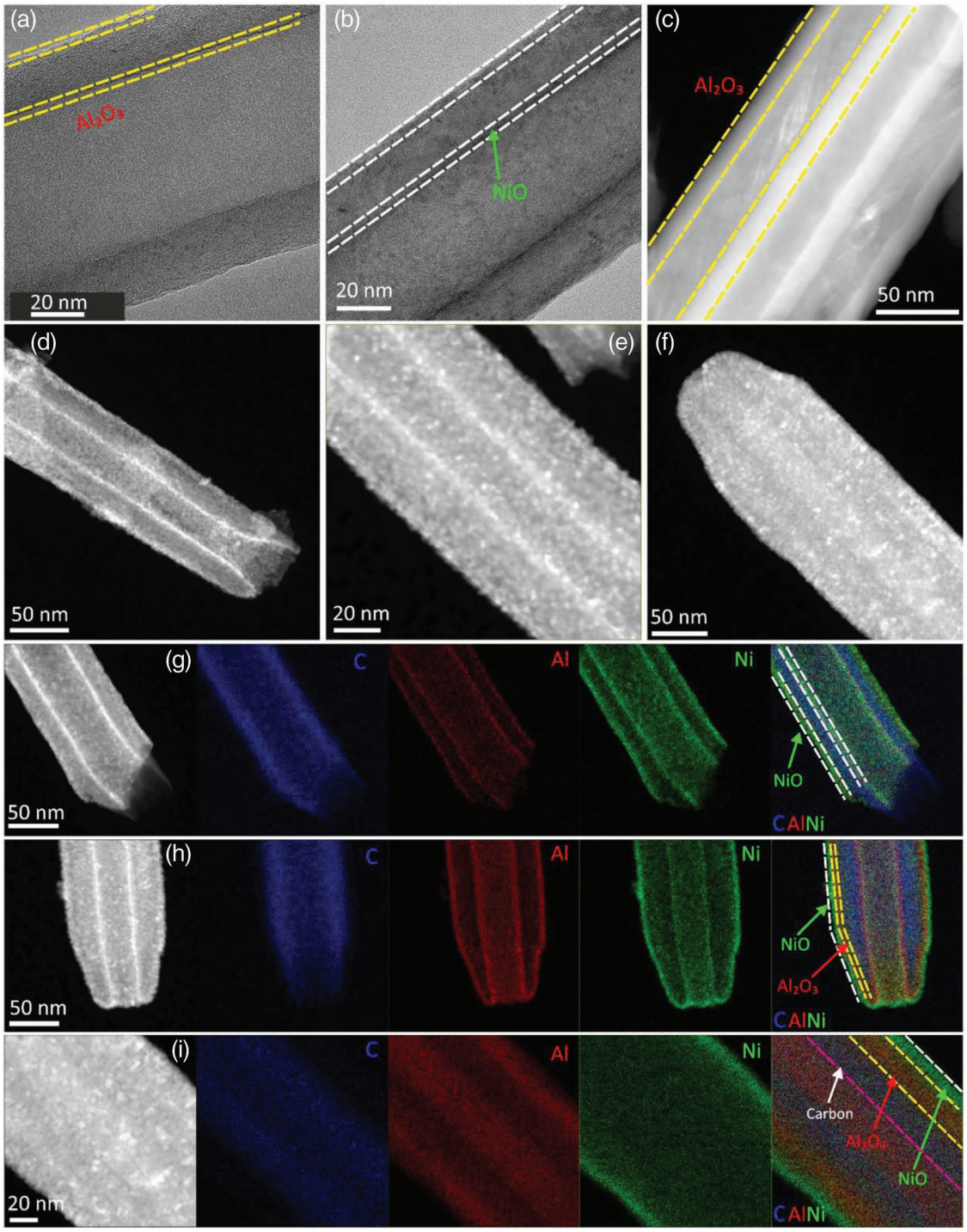

Figure 8. Bright-field TEM images for the a) $4Al_2O_3$-SCCNT and b) 200NiO-$4Al_2O_3$-SCCNT heterostructures. HAADF-STEM images for the c) $100Al_2O_3$-SCCNT, d) 200NiO-$4Al_2O_3$-SCCNT, e) 200NiO-$19Al_2O_3$-SCCNT, and f) 200NiO-$100Al_2O_3$-SCCNT heterostructures. g–i) HAADF-STEM images and the corresponding EDX elemental mappings for the 200NiO-$4Al_2O_3$-SCCNT, 200NiO-$19Al_2O_3$-SCCNT, and 200NiO-$100Al_2O_3$-SCCNT, respectively.

and the 200NiO-$4Al_2O_3$-SCCNT sample shows approximately three-order-of-magnitude higher resistance as compared to the 200NiO-SCCNT heterostructures. This indicates that electrons can cross this thinner insulating space only through the tunneling effect, as reported for Al_2O_3 layer deposited on different substrates.[30] This behavior was further confirmed (Figure 9b–d) by the measurements carried out at different potential applied (0.1–10 V). However, this behavior is expected to be decrease with increasing the Al_2O_3 film thickness, demonstrating an increase in the baseline resistance with the

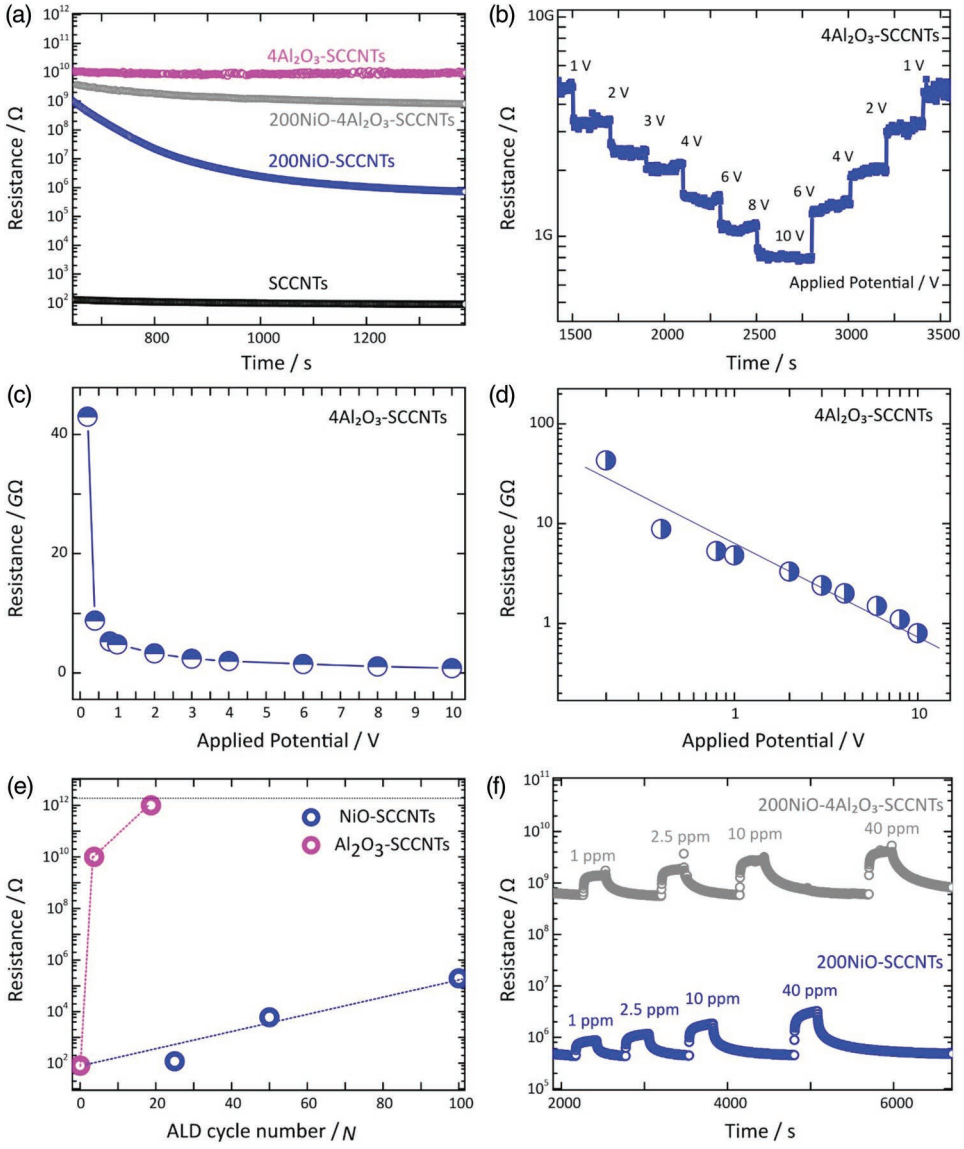

Figure 9. a) Baseline resistance of noncoated SCCNT, 200NiO-SCCNT, $4Al_2O_3$-SCCNT, and 200NiO-$4Al_2O_3$-SCCNT samples, during heating from room temperature to 200 °C in air, b–d) baseline resistance of $4Al_2O_3$-SCCNTs at 200 °C in air at different applied potentials (0.1–10 V), e) baseline resistance of YAl_2O_3-SCCNTs and XNiO-SCCNTs at 200 °C in air at an applied potential of 1 V, f) acetone sensing experiments and dynamic response toward different concentrations of acetone at 200 °C from 200NiO-SCCNTs and 200NiO-$4Al_2O_3$-SCCNTs heterostructures.

higher number of ALD cycles. So, for $Y > 4$ in XNiO-YAl_2O_3-SCCNTs heterostructures the tunneling effect cannot take place anymore and the current can only flow along the NiO polycrystalline film (**Figure 10**). As compared to NiO-SCCNTs, at the same coating thickness, the resistance of the Al_2O_3-SCCNTs is much higher due to the higher insulating character of Al_2O_3 compared to NiO. Data obtained at $V = 1$ V are summarized in Figure 9e. The top-most dotted line represents the detection limit of our instrument.

The acetone sensing experiments were further performed with the Al_2O_3-SCCNT, NiO-SCCNT, and NiO-Al_2O_3-SCCNT sensors (Figure 9f). There was no response recorded for the $4Al_2O_3$-SCCNT sensor. However, the 200NiO-SCCNT and 200NiO-$4Al_2O_3$-SCCNT sensors show a typical dynamic response toward acetone at different concentrations. It is noteworthy that there is no differences in the response and response/recovery time, indicating that the presence of thin layer of Al_2O_3, even if it drastically changes the baseline resistance, it does not modify at all the sensing performances. This means that the sensing performances are strictly related to the top sensing surface, NiO in this case, and the presence of Al_2O_3 thin layer does not interfere with the creation of the accumulation layer, in full agreement with the mechanism described above.

The dynamic response of the 200NiO-SCCNT sensor, showing the best performance was measured for 10 ppm of acetone and ethanol at 200 °C (**Figure 11**a). It shows a good repeatability and recovery of the signals after successive exposure to acetone/ethanol and air. The reproducibility of the

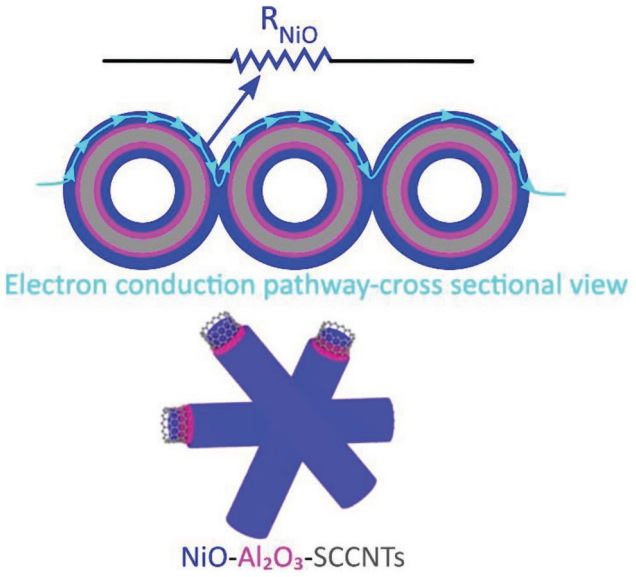

Figure 10. Schematics of the NiO-Al_2O_3-SCCNTs heterostructures and the cross-sectional view for the proposed electronic conduction channel dominating along the NiO shell for thick Al_2O_3 layers ($Y > 4$ in XNiO-$Y$$Al_2O_3$-SCCNTs heterostructures).

200NiO-SCCNT sensor was also evaluated for acetone at 200 °C. To fulfill this aim, two replicate sensors were prepared from the same samples (i.e., 200NiO-SCCNTs) and tested under similar conditions. The results reported in Figure 11b show a stable baseline resistance (no drift) and good reproducibility of the signals, indicating an acceptable performance of the fabricated sensors. The selectivity of the 200NiO-SCCNT sensor was tested against acetone, ethanol and some interfering gases like CO_2, NO_2, NH_3, CO, methane, and hydrogen. It is clear that 200NiO-SCCNT sensor shows a significant and clear response toward acetone and ethanol, whereas it shows lower effective signals for other gases, at concentrations relevant to typical gas sensing applications (Figure 11c). Hence, the 200NiO-SCCNTs fabricated sensor shows a good selectivity for acetone and ethanol detection at 200 °C. Table S1 (Supporting Information) compares the gas sensing properties of our NiO-SCCNTs core-shell heterostructures to some state-of-the-art NiO nanostructures, reported for ethanol and acetone sensing.

4. Conclusion

Gas sensing performance and mechanism are reported for NiO-SCCNTs C-S hierarchical heterostructures with a range

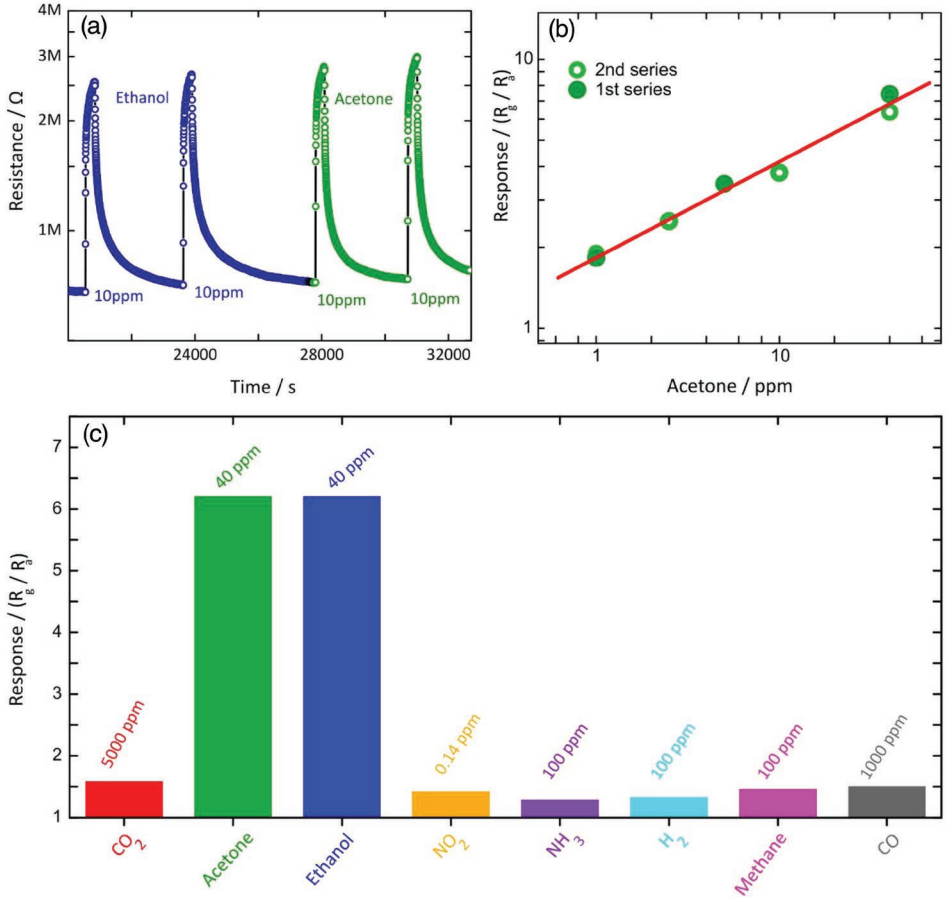

Figure 11. a) Successive response of 200NiO-SCCNTs fabricated sensor to 10 ppm of ethanol and acetone at 200 °C. b) Response of the two different sensors fabricated by 200NiO-SCCNTs toward acetone at 200 °C. c) Response of 200NiO-SCCNTs sensor to acetone, ethanol, and other gases at 200 °C, which demonstrates a good selectivity toward ethanol and acetone.

of ALD deposited ultrathin layers of NiO (from 0.80 to 21.8 nm in thickness). The modest SCCNT sensor capabilities are greatly enhanced by the homogenous and conformal coating with a NiO shell layer. Both the electrical properties and the sensor response of NiO-SCCNTs C-S hierarchical heterostructures to acetone and ethanol are strongly dependent on the thickness of the NiO shell layer, proving that the sensor performances are controlled by the ratio between the thickness of the hole accumulation layer and the total layer thickness, in the case in which the later exceeds the former. For the other case, the limited availability of free charge carriers hinders the sensing performance. Besides allowing for the formation of high quality conformal NiO layers, the presence of the very low resistivity SCCNTs cores determines a conduction path that transversally crosses the NiO shells and by that enhances the sensing performance. The 200NiO-SCCNT (6.5 nm NiO shell layer) sensors show the best performance among others due to the matching of the Debye length (λ_D) with the coating thickness. The investigations on NiO-Al_2O_3-SCCNT, Al_2O_3-SCCNT, and NiO-SCCNT coaxial heterostructures revealed that the electrical conduction mechanism at the interfaces is controlled by the NiO shell layer. The NiO-SCCNT sensors also showed excellent performance in terms of repeatability, reproducibility, and selectivity toward acetone and ethanol. The noteworthy performance of 200NiO-SCCNT sensors can be attributed to the good conductivity and high surface-area of the SCCNT substrate, the conformal and homogenous NiO coating achievable by ALD and the optimized NiO thickness. All in all, we are convinced that our optimized heterostructures endow a great potential for gas sensing applications.

Supporting Information

Supporting Information is available from the Wiley Online Library or from the author.

Acknowledgements

M.H.R. acknowledges the University of the Punjab, Lahore, Pakistan for the scholarship. Christoph Erdmann is acknowledged for TEM and Patrick Amsalem for XPS measurements.

Conflict of Interest

The authors declare no conflict of interest.

Keywords

atomic layer deposition (ALD), carbon nanotubes, dielectric interfacial layer, gas sensors, nickel oxide, shell layer thickness

Received: August 21, 2019
Revised: October 9, 2019
Published online: November 18, 2019

[1] a) T. Seiyama, A. Kato, K. Fujiishi, M. Nagatani, *Anal. Chem.* **1962**, *34*, 1502; b) G. Neri, *Chemosensors* **2015**, *3*, 1; c) I.-D. Kim, A. Rothschild, H. L. Tuller, *Acta Mater.* **2013**, *61*, 974; d) E. Comini, *Anal. Chim. Acta* **2006**, *28*, 568.

[2] a) W. Zeng, B. Miao, L.-y. Lin, J.-y. Xie, *Trans. Nonferrous Met. Soc. China* **2012**, *22*, s100; b) S. M. Majhi, G. K. Naik, H.-J. Lee, H.-G. Song, C.-R. Lee, I.-H. Lee, Y.-T. Yu, *Sens. Actuators, B* **2018**, *268*, 223; c) I. Hotovy, V. Rehacek, P. Siciliano, S. Capone, L. Spiess, *Thin Solid Films* **2002**, *9*, 418; d) J. Fang, Y. Zhu, D. Wu, C. Zhang, S. Xu, D. Xiong, P. Yang, L. Wang, P. K. Chu, *Sens. Actuators, B* **2017**, *252*, 1163.

[3] L. Xu, R. Zheng, S. Liu, J. Song, J. Chen, B. Dong, H. Song, *Inorg. Chem.* **2012**, *51*, 7733.

[4] a) B. Liu, H. Yang, H. Zhao, L. An, L. Zhang, R. Shi, L. Wang, L. Bao, Y. Chen, *Sens. Actuators, B* **2011**, *156*, 251; b) J. Wang, P. Yang, X. Wei, Z. Zhou, *Nanoscale Res. Lett.* **2015**, *10*, 119; c) Y. Ren, W. K. Chim, S. Y. Chiam, J. Q. Huang, C. Pi, J. S. Pan, *Adv. Funct. Mater.* **2010**, *20*, 3336; d) G. Zhu, C. Xi, H. Xu, D. Zheng, Y. Liu, X. Xu, X. Shen, *RSC Adv.* **2012**, *2*, 4236; e) N. D. Hoa, S. A. El-Safty, *Chem. - Eur. J.* **2011**, *17*, 12896; f) N. G. Cho, H.-S. Woo, J.-H. Lee, I.-D. Kim, *Chem. Commun.* **2011**, *47*, 11300.

[5] a) L. Wang, Z. Lou, R. Wang, T. Fei, T. Zhang, *J. Mater. Chem.* **2012**, *22*, 12453; b) L. Wang, J. Deng, T. Fei, T. Zhang, *Sens. Actuators, B* **2012**, *164*, 90; c) Y. Wang, A. Maity, X. Sui, H. Pu, S. Mao, N. K. Singh, J. Chen, *ACS Omega* **2018**, *3*, 18685.

[6] a) H.-J. Kim, K.-I. Choi, K.-M. Kim, C. W. Na, J.-H. Lee, *Sens. Actuators, B* **2012**, *171–172*, 1029; b) G. Mattei, P. Mazzoldi, M. L. Post, D. Buso, M. Guglielmi, A. Martucci, *Adv. Mater.* **2007**, *19*, 561; c) M. ul Haq, Z. Wen, Z. Zhang, S. Khan, Z. Lou, Z. Ye, L. Zhu, *Sci. Rep.* **2018**, *8*, 1705; d) J. Wang, L. Wei, L. Zhang, J. Zhang, H. Wei, C. Jiang, Y. Zhang, *J. Mater. Chem.* **2012**, *22*, 20038.

[7] a) K. Wetchakun, T. Samerjai, N. Tamaekong, C. Liewhiran, C. Siriwong, V. Kruefu, A. Wisitsoraat, A. Tuantranont, S. Phanichphant, *Sens. Actuators, B* **2011**, *160*, 580; b) S. Wang, Y. Kang, L. Wang, H. Zhang, Y. Wang, Y. Wang, *Sens. Actuators, B* **2013**, *182*, 467; c) J. Shin, S.-J. Choi, I. Lee, D.-Y. Youn, C. O. Park, J.-H. Lee, H. L. Tuller, I.-D. Kim, *Adv. Funct. Mater.* **2013**, *23*, 2357; d) X. Liu, T. Ma, N. Pinna, J. Zhang, *Adv. Funct. Mater.* **2017**, *27*, 1702168.

[8] a) P. M. Arnal, M. Comotti, F. Schüth, *Angew. Chem., Int. Ed.* **2006**, *45*, 8224; b) N. Pinna, G. Neri, M. Antonietti, M. Niederberger, *Angew. Chem., Int. Ed.* **2004**, *43*, 4345.

[9] a) C. Yujin, Z. Chunling, W. Taihong, *Nanotechnology* **2006**, *17*, 3012; b) T. Li, W. Zeng, Z. Wang, *Sens. Actuators, B* **2015**, *221*, 1570.

[10] a) P. Chandrasekhar, in *Conducting Polymers, Fundamentals and Applications: Including Carbon Nanotubes and Graphene* (Ed: P. Chandrasekhar), Springer International Publishing, Cham **2018**, p. 53; b) S.-O. Jennifer, W. Hung-Ta, S. K. Byoung, W. Zhuangchun, R. Fan, G. R. Andrew, J. P. Stephen, *Nanotechnology* **2005**, *16*, 2218.

[11] N. Chen, Q. Li, Y. Li, D. Deng, X. Xiao, Y. Wang, *J. Mater. Sci.: Mater. Electron.* **2015**, *26*, 8240.

[12] M. Catherine, D. Nicola, L. Mariangela, W. Marc Georg, T. Jean-Philippe, N. Giovanni, P. Nicola, *Nanotechnology* **2015**, *26*, 024004.

[13] a) G. Lu, L. E. Ocola, J. Chen, *Adv. Mater.* **2009**, *21*, 2487; b) C. Marichy, P. A. Russo, M. Latino, J.-P. Tessonnier, M.-G. Willinger, N. Donato, G. Neri, N. Pinna, *J. Phys. Chem. C* **2013**, *117*, 19729; c) N. Van Hieu, L. T. B. Thuy, N. D. Chien, *Sens. Actuators, B* **2008**, *129*, 888; d) N. Duc Hoa, N. Van Quy, Y. Suk Cho, D. Kim, *Phys. Status Solidi A* **2007**, *204*, 1820.

[14] C. Balázsi, K. Sedlácková, E. Llobet, R. Ionescu, *Sens. Actuators, B* **2008**, *133*, 151.

[15] J.-M. Tulliani, A. Cavalieri, S. Musso, E. Sardella, F. Geobaldo, *Sens. Actuators, B* **2011**, *152*, 144.

[16] a) M.-G. Willinger, G. Neri, A. Bonavita, G. Micali, E. Rauwel, T. Herntrich, N. Pinna, *Phys. Chem. Chem. Phys.* **2009**, *11*, 3615; b) S. Santangelo, G. Messina, G. Faggio, M. G. Willinger, N. Pinna, A. Donato, A. Arena, N. Donato, G. Neri, *Diamond Relat. Mater.* **2010**, *19*, 590; c) M.-G. Willinger, G. Neri, E. Rauwel, A. Bonavita, G. Micali, N. Pinna, *Nano Lett.* **2008**, *8*, 4201.

[17] D. Jung, M. Han, G. S. Lee, *Carbon* **2014**, *78*, 156.

[18] a) V. V. Sysoev, E. Strelcov, S. Kar, A. Kolmakov, *Thin Solid Films* **2011**, *520*, 898; b) A. Mirzaei, J.-H. Kim, H. W. Kim, S. S. Kim, *Sens. Actuators, B* **2018**, *258*, 270; c) C. Marichy, N. Pinna, *Adv. Mater. Interfaces* **2016**, *3*, 1600335; d) Z. Xu, Y. Hou, S. Sun, *J. Am. Chem. Soc.* **2007**, *129*, 8698.

[19] a) C. Marichy, A. Pucci, M.-G Willinger, N. Pinna, in *Atomic Layer Deposition of Nanostructured Materials* (Eds: N. Pinna, M. Knez), Wiley-VCH, Weinheim, Germany **2012**, p. 327; b) S. M. George, *Chem. Rev.* **2010**, *110*, 111; c) C. Marichy, J.-P. Tessonnier, M. C. Ferro, K.-H. Lee, R. Schlögl, N. Pinna, M.-G. Willinger, *J. Mater. Chem.* **2012**, *22*, 7323; d) N. Pinna, M. Knez, *Atomic layerdepositon of nanostructured materials*, Wiley-VCH, Weinheim, Germany **2011**; e) C. Marichy, N. Pinna, *Coord. Chem. Rev.* **2013**, *257*, 3232; f) C. Marichy, M. Bechelany, N. Pinna, *Adv. Mater.* **2012**, *24*, 1017; g) Y. Fan, Y. Wu, G. Clavel, M. H. Raza, P. Amsalem, N. Koch, N. Pinna, *ACS Appl. Energy Mater.* **2018**, *1*, 4554.

[20] a) C. Marichy, N. Donato, M.-G. Willinger, M. Latino, D. Karpinsky, S.-H. Yu, G. Neri, N. Pinna, *Adv. Funct. Mater.* **2011**, *21*, 658; b) N. Pinna, C. Marichy, M. G. Willinger, N. Donato, M. Latino, G. Neri, *Lecture Notes in Electrical Engineering*, Springer, Boston, MA **2012**, p. 109.

[21] M. H. Raza, K. Movlaee, Y. Wu, S. M. El-Refaei, M. Karg, S. G. Leonardi, G. Neri, N. Pinna, *ChemElectroChem* **2019**, *6*, 383.

[22] a) F. Moosavi, E. M. Bahrololoom, R. Kamjou, A. Mirzaei, G. S. Leonardi, G. Neri, *Chemosensors* **2018**, *6*, 61; b) N. Zahmouli, M. Hjiri, L. El Mir, A. Bonavita, N. Donato, G. Neri, S. G. Leonardi, *Nanotechnology* **2019**, *30*, 055502.

[23] a) D. Alders, F. C. Voogt, T. Hibma, G. A. Sawatzky, *Phys. Rev. B* **1996**, *54*, 7716; b) Y. Jiang, S. Yu, J. Li, L. Jia, C. Wang, *Carbon* **2013**, *63*, 367; c) S. Seo, I. J. Park, M. Kim, S. Lee, C. Bae, H. S. Jung, N.-G. Park, J. Y. Kim, H. Shin, *Nanoscale* **2016**, *8*, 11403; d) L. Soriano, I. Preda, A. Gutiérrez, S. Palacín, M. Abbate, A. Vollmer, *Phys. Rev. B* **2007**, *75*, 233417; e) A. G. Marrani, V. Novelli, S. Sheehan, D. P. Dowling, D. Dini, *ACS Appl. Mater. Interfaces* **2014**, *6*, 143.

[24] a) M. Awais, D. P. Dowling, F. Decker, D. Dini, *Adv. Condens. Matter Phys.* **2015**, *2015*, 186375; b) O. Diaz-Morales, D. Ferrus-Suspedra, M. T. M. Koper, *Chem. Sci.* **2016**, *7*, 2639; c) J. R. Manders, S.-W. Tsang, M. J. Hartel, T.-H. Lai, S. Chen, C. M. Amb, J. R. Reynolds, F. So, *Adv. Funct. Mater.* **2013**, *23*, 2993; d) V. Novelli, M. Awais, D. P. Dowling, D. Dini, *Am. J. Anal. Chem.* **2015**, *6*, 176.

[25] a) P. Collins, *Bull. Am. Phys. Soc.* **1999**, *44*, 1889; b) P. G. Collins, K. Bradley, M. Ishigami, A. Zettl, *Science* **2000**, *287*, 1801; c) N. Kobayashi, T. Enoki, C. Ishii, K. Kaneko, M. Endo, *J. Chem. Phys.* **1998**, *109*, 1983; d) G. U. Sumanasekera, C. K. W. Adu, S. Fang, P. C. Eklund, *Phys. Rev. Lett.* **2000**, *85*, 1096; e) Y. Wang, J. T. W. Yeow, *J. Sens.* **2009**, *2009*, 493904.

[26] F. Qu, J. Liu, Y. Wang, S. Wen, Y. Chen, X. Li, S. Ruan, *Sens. Actuators, B* **2014**, *199*, 346.

[27] a) A. Katoch, S.-W. Choi, G.-J. Sun, S. S. Kim, *J. Mater. Chem. A* **2013**, *1*, 13588; b) Q. Xu, Z. Zhang, X. Song, S. Yuan, Z. Qiu, H. Xu, B. Cao, *Sens. Actuators, B* **2017**, *245*, 375.

[28] N. Barsan, U. Weimar, *J. Electroceram.* **2001**, *7*, 143.

[29] J. Wang, Z. Zheng, D. An, X. Tong, Q. Zhou, *Mater. Sci. Semicond. Process.* **2018**, *83*, 139.

[30] a) M. D. Groner, J. W. Elam, F. H. Fabreguette, S. M. George, *Thin Solid Films* **2002**, *413*, 186; b) P. A. Packan, *Science* **1999**, *285*, 2079.